Inertial-Fusion-Related Hydrodynamic Instabilities in a Spherical Gas Bubble Accelerated by a Planar Shock Wave

J. Niederhaus, D. Ranjan, M. Anderson, J. Oakley, R. Bonazza, J. Greenough

September 2004

UWFDM-1240

Presented at the 16th ANS Topical Meeting on Fusion Energy, 14–16 September 2004, Madison WI.

FUSION TECHNOLOGY INSTITUTE

UNIVERSITY OF WISCONSIN

MADISON WISCONSIN

Inertial-Fusion-Related Hydrodynamic Instabilities in a Spherical Gas Bubble Accelerated by a Planar Shock Wave

J. Niederhaus, D. Ranjan, M. Anderson, J. Oakley, R. Bonazza, J. Greenough

Fusion Technology Institute
University of Wisconsin
1500 Engineering Drive
Madison, WI 53706

http://fti.neep.wisc.edu

September 2004

UWFDM-1240

Presented at the 16th ANS Topical Meeting on Fusion Energy, 14–16 September 2004, Madison WI.

INERTIAL-FUSION-RELATED HYDRODYNAMIC INSTABILITIES IN A SPHERICAL GAS BUBBLE ACCELERATED BY A PLANAR SHOCK WAVE

John Niederhaus, Devesh Ranjan, Mark Anderson, Jason Oakley, Riccardo Bonazza, Jeff Greenough*

University of Wisconsin-Madison, Department of Engineering Physics
1500 Engineering Drive, Madison, WI 53706
bonazza@engr.wisc.edu
**Lawrence Livermore National Laboratory*
Livermore, CA 94550

Experiments studying the compression and unstable growth of a dense spherical bubble in a gaseous medium subjected to a strong planar shock wave ($2.8 < M < 3.4$) are performed in a vertical shock tube. The test gas is initially contained in a free-falling spherical soap-film bubble, and the shocked bubble is imaged using planar laser diagnostics. Concurrently, simulations are carried out using a compressible hydrodynamics code in r-z *axisymmetric geometry.*

Experiments and computations indicate the formation of characteristic vortical structures in the post-shock flow, due to Richtmyer-Meshkov and Kelvin-Helmholtz instabilities, and smaller-scale vortices due to secondary effects. Inconsistencies between experimental and computational results are examined, and the usefulness of the current axisymmetric approach is evaluated.

I. BACKGROUND

In laser, heavy-ion, or Z-pinch-driven ICF ignition, compression of the target is accompanied by fluid instability growth. This instability is key to the understanding of the ignition and yield from the target. The surface of the DT target becomes unstable due to Rayleigh-Taylor and Richtmyer-Meshkov[1,2] growth. Vorticity is generated baroclinically at the interface, causing the interface to deform and allowing the materials to mix after the shock has passed. This turbulent mixing between the DT and the ablator surface, and the asymmetry associated with the compression, can alter the yield from the target.

Shock tube experiments are currently underway at the University of Wisconsin-Madison in an effort to characterize the growth of these instabilities, for the special case of a dense spherical bubble. The high structural capacity of the shock tube facilitates experiments at Mach numbers exceeding those achieved in previous hydrodynamic shock-induced-mixing experiments.

Richtmyer-Meshkov and Kelvin-Helmholtz instabilities on the bubble surface lead to the formation of large vortical structures in the post-shock flow. As the incident planar shock wave passes over the bubble, it deposits vorticity on its surface. This is a "baroclinic" process: vorticity deposition is proportional to the cross product of the pressure and density gradients. Therefore, the strongest vorticity deposition is at the bubble circumference where the surface is tangent to the incident shock pressure gradient.[4] This produces a strong vortex ring that entrains the bubble gas and dominates the post-shock flow.

The sense of the vorticity depends on the sign of the cross product, and thus on the direction of the density gradient. These experiments study the "heavy bubble" case, in which the density gradient is oriented radially inward, and the vortex ring consequently forms in the "stagnant" or "backward" configuration shown below in Figure 1.

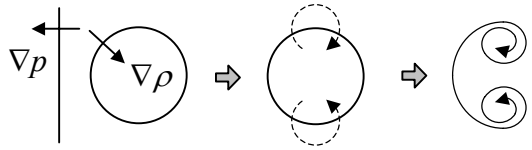

Fig. 1. Baroclinic vorticity deposition on the surface of a heavy bubble in a light gas by a planar shock wave.

A number of past experiments have examined the shock bubble interaction, either in spherical or cylindrical geometry.[3-7] These typically fall into two categories. One set includes experiments carried out in gas-driven shock tubes. These experiments are limited to shock strengths $M < 1.3$, but provide a clear view of hydrodynamic shock-induced mixing, without the additional effects of phase changes and electromagnetic fields. The other set includes experiments carried out in laser-driven shock tubes. These are characterized by very high Mach numbers ($M > 10$) and density ratios. The current set of experiments examines a shocked bubble at $M = 2.88$, in an attempt to gain understanding in a regime well above

the previous low M shock tube experiments and well below the shock strengths achieved in laser-driven experiments.

II. SHOCK TUBE EXPERIMENTS

II.A. Wisconsin Shock Tube Laboratory

The shock-bubble interaction is studied at these intermediate Mach numbers in the Wisconsin Shock Tube Laboratory (WiSTL) 9-meter vertical shock tube, at the University of Wisconsin-Madison.[8,9] The shock tube facility is designed to produce a strong, uniform, planar shock wave, which travels from top to bottom and interacts with experiments set up in a test section at the bottom of the duct. The shock is generated by bursting a steel diaphragm near the head of the duct, and its strength is controlled by selecting an appropriate diaphragm thickness. A fast-acting solenoid valve controls the driver, so that the timing of diaphragm rupture can be controlled to within approximately 100 ms. The duct has a 25.4-cm square internal cross section, with walls of steel and reinforced concrete. This gives the WiSTL facility an impulsive load capability of 20 MPa, allowing the use of shock strengths up to approximately $M = 4$ (in nitrogen).

II.B. Bubble Generation

For these experiments, a retractable bubble dropper was added to the shock tube. This mechanism places a bubble in free fall in the center of the duct and is quickly retracted into a slot in the side wall, allowing the shock to pass without flow obstruction. In its retracted position, the mechanism is protected from shearing by the shocked flow, allowing it to be used repeatedly in successive experiments. The design of this mechanism is shown below schematically in Figure 2.

A bubble is generated for each experiment by applying a soap film of appropriate thickness to the dropper head and flowing a specified volume of test gas into the dropper, causing a bubble of the desired size to appear. For the current experiments, the selected test gas is heavy relative to the ambient gas. Thus, the action of retracting the dropper causes the bubble to release by inertia and subsequently to move in free fall until it is overtaken by the incident shock wave. The generation of the shock wave is automatically triggered by the dropper retraction, and the delay time between bubble generation and shock interaction is minimized.

The current experimental campaign uses a bubble diameter of approximately 5 cm. The bubble gas is argon, and the driven gas is nitrogen, initially at atmospheric pressure and room temperature. This results in a pre-shock Atwood number $A = 0.176$. The soap film is estimated to be 0.5 μm thick (on average), although some nonuniformities are known to exist on both the interior and exterior of the film. These include droplets of film material remaining inside the bubble, and excess film material sagging from the exterior at the bottom of the bubble. The total mass of the bubble film material is estimated to be less than 10% of the mass of the bubble interior gas.

II.C. Planar Laser Diagnostics

The shocked bubble is imaged with a laser sheet produced using a Q-switched Nd:YAG laser (Continuum Surelite II). The beam is formed into a plane and transmitted through a port centered in the shock tube endwall. Two 10-ns pulses are used in each experiment, separated by a specified delay time. The resulting scattered light is captured by a 1024×1024 Andor CCD camera. Thus, two images of the post-shock bubble are acquired on a dual-exposure frame in each experiment.

With timing selected to capture the bubble at a certain point in its development, the imaging laser enters from the bottom of the shock tube and intersects the shocked bubble near its midplane, as shown in Figure 2. Mie scattering from atomized film material in the plane of the laser sheet produces an image of the shocked bubble, which is projected through a port in the side wall and recorded. The long-term evolution of the instability is thus studied by the coupling of multiple experiments. The initial condition is easily reproducible, with bubble diameter $D = 5.00 \pm 0.02$ cm and shock strength $M = 2.88 \pm 0.04$.

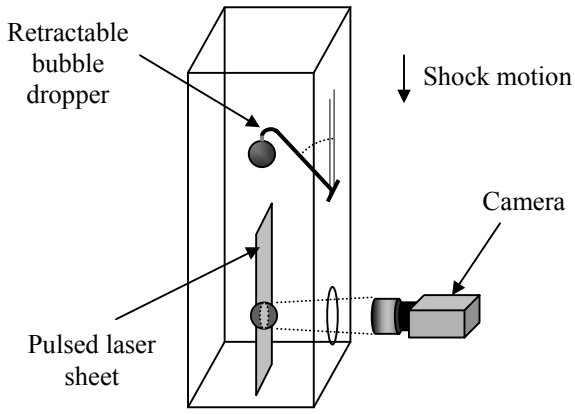

Fig. 2. Schematic setup for shocked bubble experiments using planar laser imaging at WiSTL.

III. HYDRODYNAMIC SIMULATIONS

Along with the shock tube experiments, hydrodynamic computations are carried out in an effort to produce a detailed simulation of the observed shock-bubble interaction. These computations are performed using a 2-D hydrodynamics code (RAPTOR) that solves the multi-

fluid compressible Navier-Stokes equations, with a perfect-gas equation of state. A shock-capturing scheme with a higher-order Godunov solver is used to handle shock propagation accurately in the calculations, and to suppress spurious oscillations near the discontinuity. RAPTOR uses a fixed (Eulerian) grid, with 2-D (r-z) axisymmetry (azimuthal variations are thus excluded) and adaptive mesh refinement (AMR), but no interface tracking. For this set of calculations, three levels of AMR are applied, with ratios 4, 4, and 2, in order to achieve high resolution of the fluid interfaces.

The initial condition, shown in Figure 3, includes a spherical argon bubble (square grid cells) suspended at rest in a quiescent nitrogen atmosphere, with a planar shock of strength $M = 2.86$ approaching from above.

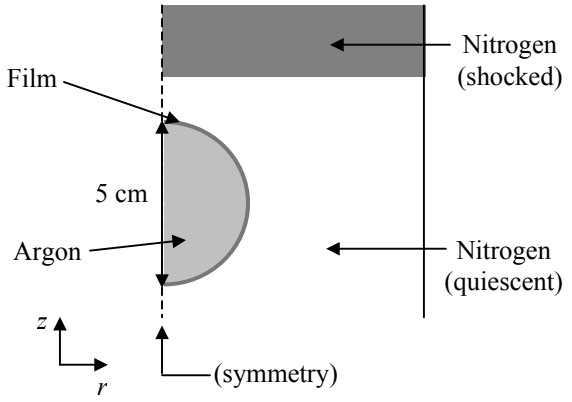

Fig. 3. Schematic setup of initial condition for simulations of shocked bubble experiments (region of interest only).

At the finest level of AMR, a mesh size of 94 μm is achieved. This gives approximately 270 mesh points per bubble radius (R_{270}). Because this is not fine enough to resolve the film thickness, the film region is modeled as a one-cell-thick spherical shell (on the finest AMR level), with density (nominally 1 g/cm^3) reduced sufficiently to give a film-to-gas mass ratio of approximately 0.1. To mitigate the effects of the "stairstepped" shape of the bubble on square grids cells, corners on the film region are smeared over one adjacent cell. This sufficiently reduces grid-seeded vorticity generation during shock passage, so that it is negligible relative to the baroclinically generated vorticity.

For the purpose of comparison to experimental images, the Ar volume fraction is plotted inside a small region of interest around the bubble. Although experimental imaging is done via scattering from film material, the images provide an outline of the shocked bubble shape, which can be visually compared to computational results. From the Ar volume fraction plots, the maximum streamwise and transverse dimensions of the shocked bubble can also be extracted and compared to experimental results.

IV. SHOCKED BUBBLE DEVELOPMENT

The experimental and computational results for the shocked bubble are compared in Figure 4(a-b). Computational images are plots of Ar volume fraction, reflected across the z-axis; experimental images represent light scattered from atomized film material in the bubble midplane.

To facilitate analysis and comparison with results from experiments at other Mach numbers, a characteristic time τ is selected. This time is the so-called "cloud-crushing time," defined as $\tau = D/u_p$, where D is the initial diameter of the bubble (5 cm), and u_p is the particle speed behind the incident shock.[5,7] For a Mach 2.86 shock, the characteristic time is $\tau = 68$ μs. Both the real time t relative to initial shock-bubble contact and the normalized time t/τ are noted in Figure 4(a-b).

The sequence shown in Figure 4(a-b) highlights the formation of a "backward" vortex ring in the post-shock flow. In both experimental and computational results, this is the dominant feature. At $t = 65$ and 70 μs, small perturbations can be seen developing on the outer limbs

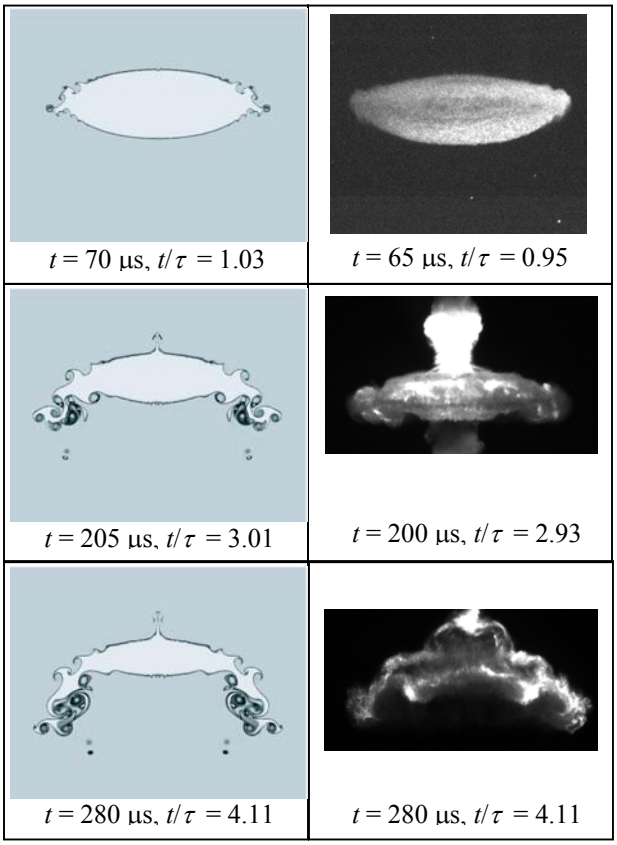

Fig. 4(a). Computational (left) and experimental (right) results for a spherical soap-film bubble of Ar in N_2, shocked at $M = 2.88$, at early times.

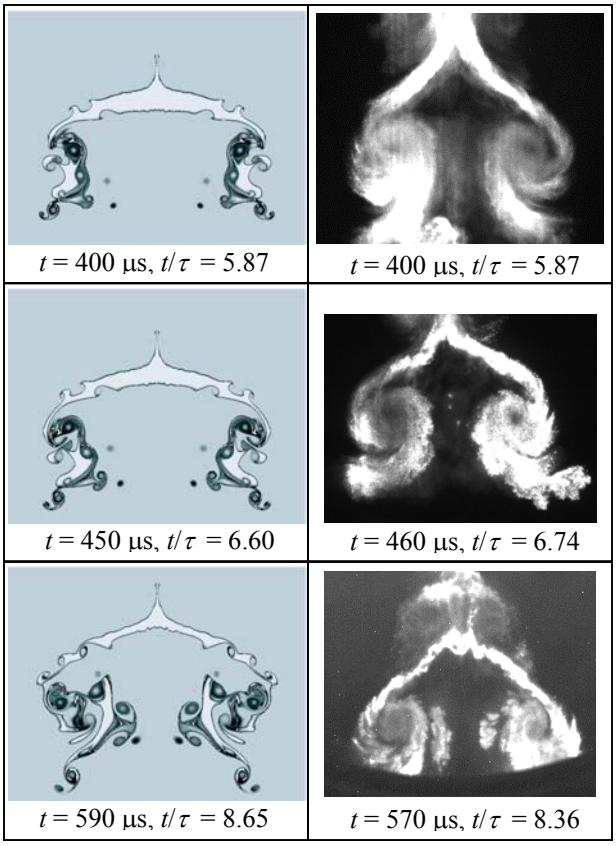

Fig. 4(b). Computational (left) and experimental (right) results for a spherical soap-film bubble of Ar in N_2, shocked at M = 2.88, at later times.

of the bubble. These are the manifestation of baroclinic vorticity generation, which is strongest on the bubble surfaces tangent to the flow direction. As time progresses, the perturbations develop into a large vortical structure on the downstream end of the bubble. Its rotation appears to be in the backward sense (motion on axis is against the flow direction).

Also, the bubble is strongly compressed in the axial direction at this point, due to inertia and increased pressure in the post-shock flow. In the first and second images in Figure 4(a), it can be observed that the elliptical shape of the compressed bubble is duplicated closely in experiment and simulation. Small vortical divots are also seen on the upper and lower surface of the compressed bubble at t = 200 μs at roughly ¾ of its full radius, and these are seen in both experiment and simulation.

A smaller secondary jet structure also appears on the upstream end of the bubble at around t = 200 μs, in both experiment and simulation. It is clear from experiments that the size and shape of this secondary jet is not repeatable, nor does it resemble that seen in simulations. Thus it may be due to artifacts of the experimental conditions, which are not accounted for in the simulation.

As time progresses, the agreement between experiment and simulation deteriorates further. At t = 280 μs, vortices on the underbelly of the shocked bubble strongly deform its elliptical shape, and a new vortical structure appears on the upper surface. Neither of these features is duplicated in the simulation.

The structure of the dominant vortex ring, as seen in the experiment, takes on a shape that is not apparent in the simulation. At t = 280 and 400 ms, the vortex ring develops in the experiment as a single large, distinct, and somewhat diffuse roll-up. In the simulation, on the contrary, multiple compact vortex rings can be seen at these times, with numerous growing perturbations on smaller scales as well. In both cases, however, it can be observed that this dominant vortical structure entrains most of the bubble gas, rolling it up vortically at the downstream end, and thus re-expanding the bubble axially after its initial compression. This becomes even more apparent at the late-time images (t = 450, 460, 590, 570 μs), where the dominant vortex ring becomes particularly large and distinct in the experimental pictures.

It is postulated that the apparent differences between the vortical structure that develops at late time in experiment and in simulation is due to subtle effects of 3-D vorticity transport. In 2-D simulations, the only vortex interaction mode is pairing. However, in the experimental flow, vortices also interact via stretching and bending modes. These additional modes may serve to suppress the development of the multiple compact, paired vortex rings that are seen in the current axisymmetric calculations.

Further, the effect of the coarse modeling of the liquid film region is not yet clear, and this may also account for some of the observed difference. Preliminary grid resolution studies indicate that if the film mass is conserved while the mesh is refined, the development of numerous discrete, paired vortices only becomes more pronounced at higher resolution. Thus, the current "smeared" model is appropriate for 2-D simulations.

Although the images at t = 400 and 460 μs are clipped, in the final experimental image (t = 570 ms), the upstream, secondary vortex ring is clearly visible. This structure grows in time and sheds additional visible vortices at its upper end. This feature becomes increasingly important at late times, but the current simulation does not duplicate it. In order to study the late-time development of the shocked bubble, it will be necessary to account for this feature, most likely by including internal and external bubble film nonuniformities in the initial condition.

V. GROWTH TRENDS / PARAMETERIZATION

In order to study the compression and unstable growth of the bubble, the transverse and axial dimensions of the bubble are measured over time and compared to the corresponding values extracted from numerical results.

The bubble "width," W, represents its maximum cross-stream dimension, and the "height," H, its maximum streamwise dimension. The data are normalized by the initial bubble diameter, D, and plotted on the dimensionless time scale t/τ, in Figures 5 and 6.

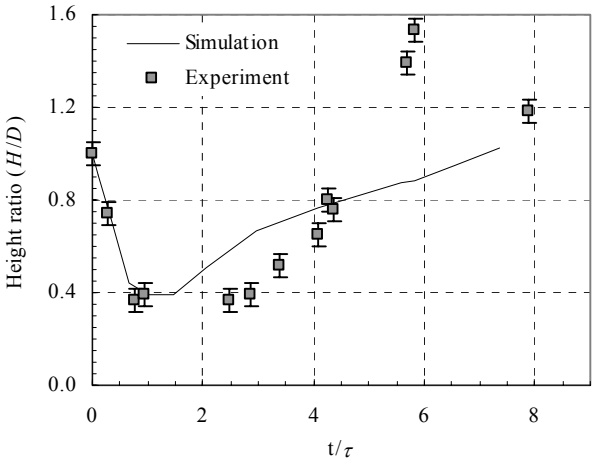

Fig. 5. Bubble width data, parameterized by $\tau = D/u_p$.

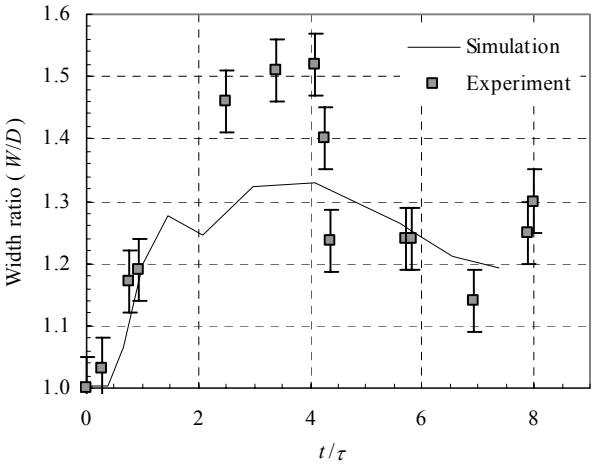

Fig. 6. Bubble height data, parameterized by $\tau = D/u_p$.

The growth trends plotted in Figure 5 show that, axially, the bubble is first compressed by the passing shock, and subsequently re-expanded by vortex effects. This re-expansion is much stronger and faster in experiment than in the simulation. This is most likely due to the secondary jet and vortex ring, and to 3-D vorticity transport effects in the dominant vortex ring.

The transverse growth trends plotted in Figure 6 show that while the bubble is compressed axially it simultaneously expands laterally. The simulation predicts that the width reaches a maximum and has a subsequent gentle decline, but experiment shows that the bubble width grows very rapidly, reaches a peak, and then abruptly declines after $t/\tau = 4$. The rapid growth and re-compression can most likely be attributed, again, to 3-D vortex effects, and to effects of the shock tube side walls.

VI. CONCLUSIONS

The present work represents a novel experimental approach, which takes advantage of planar imaging, high shock strengths relative to previous shock tube experiments, and a flow that is unobstructed by bubble holders or injectors. This approach facilitates the observation of the large characteristic vortex ring that forms in the post-shock flow due to fluid instabilities, as predicted in theory and observed in simulations.

However, it is clear from these results that further detail is needed in the numerical simulation of the shocked bubble experiments. Significant inconsistencies between experiment and simulation exist in both the bubble/vortex ring morphology and in the rate of instability growth. These inconsistencies are attributed to coarse bubble film modeling and to the subtle differences between 2-D (axisymmetric) and 3-D vortex interactions.

ACKNOWLEDGMENTS

This work was performed under the auspices of the U.S. Department of Energy by University of California Lawrence Livermore National Laboratory under contract No. W-7405-Eng-48.

REFERENCES

[1] R. D. RICHTMYER, Comm. on Pure and App. Math. **13**, 297 (1960).

[2] Y. Y. MESHKOV, NASA Technical Translation **NASA TT F-13,074** (1970).

[3] J.-F. HAAS and B. STURTEVANT, *J. Fluid Mech.*, **181**, 41 (1987).

[4] J. W. JACOBS, *Phys. Fluids A*, **5 (9)**, 2239 (1993).

[5] H. F. ROBEY, T. S. PERRY, R. I. KLEIN, J. O. KANE, J. A. GREENOUGH, and T. R. BOEHLY, *Phys. Rev. Let*, **89**, 085001 (2002).

[6] C. A. ZOLDI, Ph.D. Thesis, SUNY Stony Brook, 2002.

[7] R. I. KLEIN, K. S. BUDIL, T. S. PERRY, and D. R. BACH, *Astrophysical Journal*, **583**, 245 (2003).

[8] M. H. ANDERSON, B. P. PURANIK, J. G. OAKLEY, and R. BONAZZA, *Shock Waves*, **10**, 377 (2000).

[9] B. P. PURANIK, J. G. OAKLEY, and M. H. ANDERSON, and R. BONAZZA *Shock Waves*, **13**, 413 (2004).